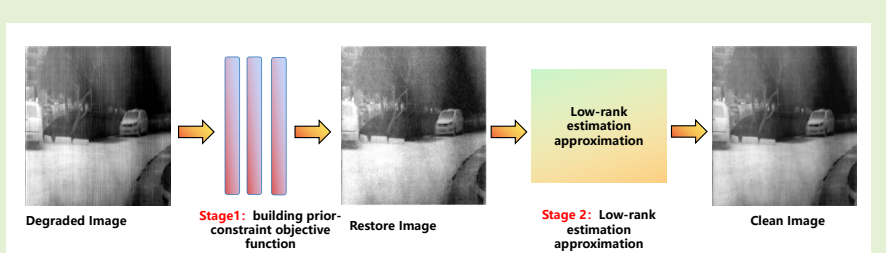


Multi-stage non-uniformity correction pipeline for single-frame infrared images based on hybrid high-order directional and low-rank prior information

Chenhua Liu ,Hao Li, Maoyong Li ,Lei Deng, Mingli Dong and Lianqing Zhu

Abstract— High-quality infrared images are widely used in various vision tasks. To address the problems of insufficient estimation and neglect of environmental noise in non-uniformity correction (NUC) methods for infrared images, we propose a new a multi-stage single-frame NUC pipeline. Firstly, for the low-rank property of infrared degraded images and the higher-order directional prior information of stripe noise, we construct an objective function which combines a higher-order gradient total variation model with a diagonal kernel paradigm as a constraint term. Multiple subproblems are solved by the alternating direction multiplier method (ADMM) to obtain the recovered image after removal of stripe. Then, we incorporate the environmental noise into the pipeline by low-rank matrix approximation and employ singular-valued patch decomposition to efficiently separate the clean image from the noise. Extensive experiments are conducted on existing methods on real and simulated datasets, and the potential performance of the proposed method is verified in qualitative and quantitative evaluations. The code and datasets can be obtain at <https://github.com/ImageVisioner/InfraredNUC>.



Index Terms— Infrared Image, Non-Uniformity Correction, Low-Rank, Higher-Order Directional , Priori Information .

I. INTRODUCTION

WITH its unique advantages, infrared thermal imaging systems have been widely used in the field of imaging systems, covering important tasks such as autonomous driving, maritime rescue, urban traffic management, industrial inspection, and reconnaissance activities [1], [2]. Among them, the infrared focal plane array (IRFPA) plays a crucial role in the conversion of thermal radiation signals to electrical signals [3], [4]. However, when the IRFPA receives the same infrared radiation, due to defects in the array material and limitations in

This work is supported by the Research Project of Beijing Municipal Natural Science Foundation (No. BJXZ2021-012-00046). Mingli Dong (Corresponding author). Author is with the Beijing Information Science and Technology University, Beijing, China (e-mail: dongm@bistu.edu.cn). Lei Deng (Corresponding author). Author is with the Beijing Information Science and Technology University, Beijing , China (e-mail:dally211@163.com). Lianqing Zhu. Author is with the Beijing Information Science and Technology University, Beijing , China (e-mail: lqzhu_bistu@sina.com). Chenhua Liu. Author is with the Beijing Information Science and Technology University adn Guangzhou Nansha Intelligent Photonic Sensing Research Institute, (e-mail: liuchenhua023@163.com). Hao Li. Author is with the Beijing Information Science and Technology University, BeiJing, China (e-mail: lh_010625@163.com). Maoyong Li. Author is with the Beijing Information Science and Technology University and Guangzhou Nansha Intelligent Photonic Sensing Research Institute, (e-mail: limaoyong@bistu.edu.cn).

Chenhua Liu and Hao Li contributed equally to this work.

the manufacturing process, the output of each detection unit may be inconsistent, resulting in non-uniform pixel response and severe spatial fixed pattern noise (FPN) [5]. At the image level, this noise manifests as interference from stripe noise and environmental noise, which has a significant negative impact on the visual quality of the image. It also has adverse effects on downstream vision tasks such as infrared small target detection [6], [7], semantic segmentation [8], image fusion [9]–[11], and target tracking [7]. Therefore, NUC can improve the quality of infrared images captured by IRFPA, which is challenging

NUC methods can be mainly divided into reference-based and scene-based methods [2], [12]. Reference-based correction methods rely on a uniform reference scene, such as a blackbody radiation source, to achieve accurate calibration of the detector response. This method aims to minimize the inconsistency of the detector response, quantifying and correcting it through the NUC coefficient. However, its reliance on a standard radiation source limits its application in certain environments, such as extreme temperature conditions or the lack of a stable reference source. In the early , scene-based methods mainly used prior information and statistical characteristics of images for FPN correction without relying on external equipment [13]–[15]. These methods rely on global motion correlation

between consecutive frames to estimate FPN in real time. However, in image sequences, when the scene motion is insufficient, artifacts are prone to occur. More, computational complexity and restrictions on relative scene motion limit the development of FPN correction using multi-frame information [12], [15]. Therefore, the NUC method based on single-frame has received extensive attention from researchers. However, these methods fail to fully consider that the image non-uniformity is not only caused by stripe noise, but also includes multiple factors such as environmental noise. Currently, single-frame NUC

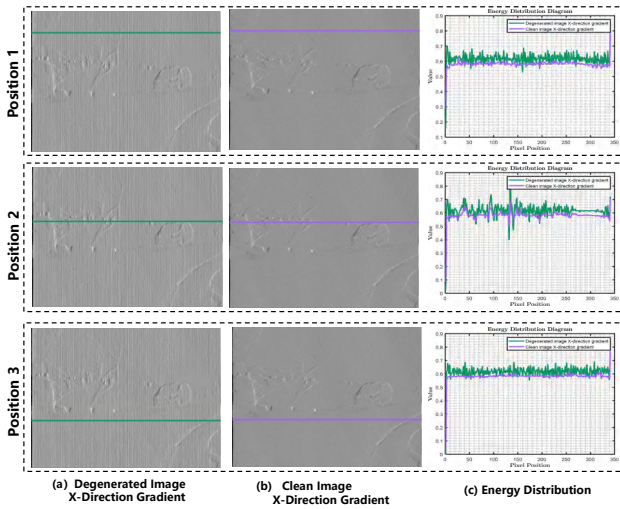


Fig. 1. Comparison of pixel intensity distribution of the gradient of the degraded image at different horizontal positions.

methods focus mainly on correcting infrared images with stripe noise [3], [16], [17]. Previously, researchers used the statistical distribution characteristics of uniform noise responses to rearrange image pixels through methods such as the Fourier transform and median histogram equalization to obtain restored images [2], [5], [18]. Filter-based methods are widely used for stripe noise capture, especially the NUC method of 1D-GF [19], which can effectively capture stripe noise. Wavelet principal component analysis and weighted least squares model optimize noise estimation and improve NUC performance [20]. Lei et al. [5] combined the interval gradient adaptive algorithm with 1D-GF to dynamically adjust the stripe noise separation and obtain accurate correction. The filtering method has obvious advantages in real-time processing, but it is easy to produce artifacts. Zuo et al. [21] proposed a bilateral filter method to suppress artifacts. Li et al. [22] developed a temporal high-pass filter method based on bilateral filter to accurately correct stripe images.

The optimization-based method utilizes the characteristics of the non-uniform image itself, regards the stripe removal task as an inverse problem, integrates the prior knowledge of the image or stripe noise into the objective function, and solves it to restore the image [3], [23], [24]. Bouali et al. proposed a variational model based on the stripe direction characteristics [25]. Based on this, Chang et al. proposed the ASSTV model to remove stripe noise

using spectral spatial information [26]. KIM et al. [3] proposed the ADOM model. The model uses a weight-based detection strategy that can effectively identify and capture stripe noise components, and adopts an acceleration strategy based on the alternating direction multiplier method to achieve rapid removal of stripe noise. Learning-based methods have been widely proposed, aiming to extract deep features of streak noise through supervised learning [27], [28]. Early models attempted to remove stripe noise by constructing shallow convolutional neural network structures [27]–[29]. However, these methods encountered challenges in capturing the semantic information of stripe components and image background, which led to artifacts when restoring images. With the introduction of ResNet [30], network structures with stronger deep fitting capabilities were developed for estimating stripe noise. Then, researchers proposed a network structure combining multi-scale fusion [31]–[33] and attention mechanism [34]–[36] to correct images contaminated by stripes. The method of using adversarial networks can effectively simulate the distribution of stripes and convert degraded images into clear images [37]. In addition, some studies have integrated noise response characteristics into neural networks to predict the distribution of stripes. At present, many research works are dedicated to combining wavelet transform and Fourier transform with convolutional neural networks to construct differentiable image correction modules [33].

Traditional stripe removal methods rely on building a priori models of degraded images and backgrounds, involving filter data statistics and optimization techniques. However, these methods cannot distinguish stripe noise from image background details, resulting in blurred vertical edges when removing stripe noise. Optimization-based methods fail to fully utilize high-order information and are insufficient in utilizing the directionality and structural characteristics of stripes, limiting the thoroughness of stripe removal. Learning-based methods rely on paired stripe-degraded images and clear images, which are difficult to obtain in real scenes. This type of method aims to achieve instant image restoration through an end-to-end training strategy, but has high requirements for computing resources. However, these methods fail to fully consider that the image non-uniformity is not only caused by stripe noise, but also includes multiple factors such as environmental noise.

Inspired by the above, we proposed a single-frame NUC pipeline for infrared images. In Fig 1 , 2 ,3 and 5 , we found that stripe noise has directional heterogeneity and low-rank characteristics, which are used to highlight the stripe components, and the objective function is constructed accordingly. Subsequently, the ADMM algorithm [38] is used to solve the optimal solution and restore a clear image. In addition, the low-rank matrix approximation theory is introduced to take environmental noise into consideration, and the clean image is separated from the environmental noise through singular value patch decomposition. Therefore, we constructed a multi-stage NUC pipeline, and its

overall framework is shown in Fig 4.

The main contributions of our research can be summarized as follows.

- We have designed a multi-stage pipeline for single-frame NUC in IRFPA images, which utilizes the directionality and low-rank characteristics of infrared stripes and environmental noise to estimate clean images from degraded images.
- In the first stage, considering the low-rank characteristics of degraded images and stripes, we construct an optimization model to generate restored images by implementing the total variation of high-order directions and the diagonal nuclear norm as regularization constraints.
- In the second stage, given that environmental noise was not taken into account in the design optimization model, this work applied low-rank matrix estimation to the processing of degraded images, in order to remove the influence of noise factors and clean the images.
- To facilitate follow-up research, we provide accessible simulation codes and simulation datasets covering various types of non-uniform noise. In addition, extensive experiments verify the potential performance of our method.

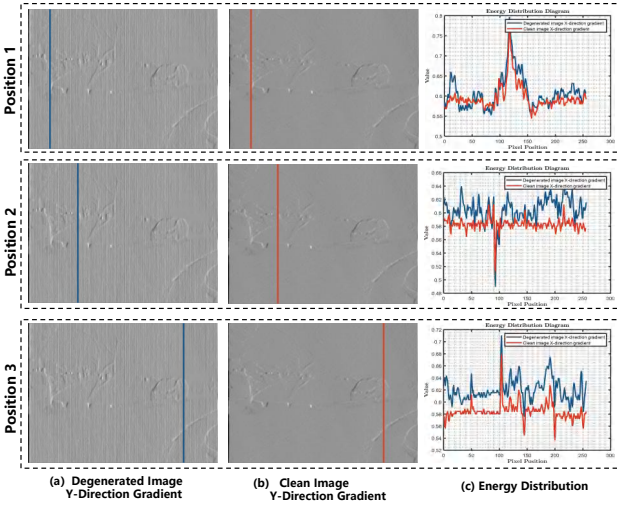


Fig. 2. Comparison of pixel intensity distribution of the gradient of the degraded image at different vertical positions.

II. RELATED WORK

In this section, we will briefly introduce methods for correcting non-uniformity in infrared images of different categories, including those based on traditional-based, optimization-based method and learning-based method.

A. Traditional-based Non-uniformity Correction Method For Images

Traditional methods mainly rely on prior knowledge of the structural features present in stripes, environmental noise and image background. These methods can be

further subdivided into statistics-based, filter-based and optimization-based methods [1], [3]. Filter-based methods often use Fourier transform or wavelet decomposition techniques to implement processing in the spatial domain or transform domain. In the early , researchers used the statistical distribution characteristics of uniform noise responses to rearrange image pixels by methods such as Fourier transform and median histogram equalization to obtain restored images. Chen [39] and Liu [40] et al. others used the Fourier transform method to remove stripe noise in the frequency domain. Torres [41], Chen [42] et al. used wavelet decomposition method to correct the non-uniformity of stripe direction attributes. Then, Cao et al. [19] used one-dimensional row-guided filters and column-guided filters to derive the behavioral patterns and high-frequency information of stripe noise to obtain a clean image. Lei [5] et al. regarded stripe noise as a "special" texture, used one-dimensional guided filtering (1D-GF) to separate the initial noise, and modified the gradient adaptively. The cascaded wavelet-fourier transform can also improve the effect of correcting non-uniform images [43], [44]. Tendero et al. [18] used the median histogram equalization method to rearrange the pixels of images with similar statistical distribution of non-uniform noise responses to obtain a clean image. By taking advantage of the statistical characteristics of the noise image, the stripe noise can be effectively and quickly eliminated; however, due to its reliance on the reference image, this method has certain limitations in performance [17], [45]. Different from the learning-based method, the optimization-based method can achieve good denoising effect on a single image [1], [3], [46].

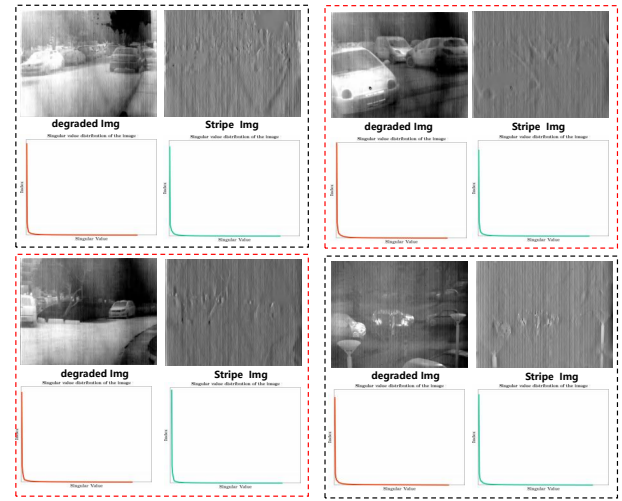


Fig. 3. Schematic diagram of the singular value distribution of degraded images and stripe noise. We can see that both degraded images and stripe noise have the characteristics of low-rank matrices.

B. Learning-based Non-uniformity Correction Method For Images

Recently, learning-based method has achieved remarkable results in the field of infrared image non-uniformity

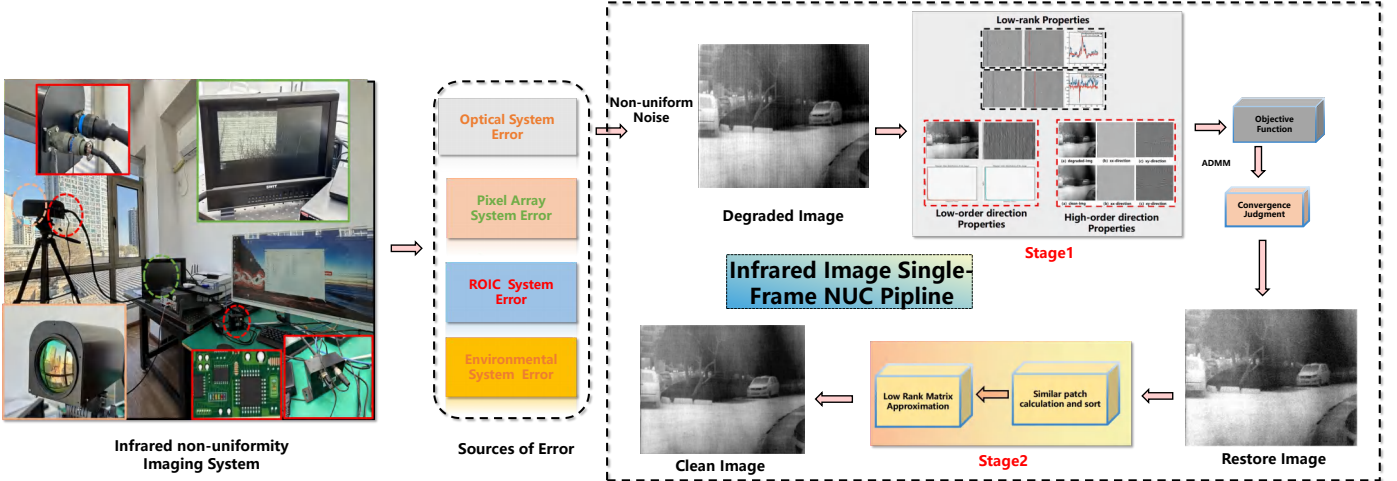


Fig. 4. The framework diagram of the NUC pipeline we proposed. We introduced the origin of non-uniform noise, then introduced stage 1 to remove stripe noise, stage 2 to remove environmental noise, and finally obtained clean image.

correction [33], as it can characterize nonlinear noise as a probability problem and effectively extract deep features [37], [47], [48]. In the early, the learning-based non-uniformity correction method realized the correction of infrared images by constructing a shallow convolutional neural network. Kuang et al. [27] first proposed a convolutional neural network (CNN) model specifically for removing stripes and improving resolution. Subsequently, He et al. further proposed a deep learning-based stripe non-uniformity correction (DLSNUC) model [47], which relies on an end-to-end deep residual network architecture and incorporates a noise simulation model to achieve accurate estimation of infrared images. These methods can capture the semantic information of the stripe components and the background, which results in standing waves. To address this issue, researchers enhance feature representation using residual learning and multi-scale strategies [31], [32]. Xiao et al. [28] adopted a local-global residual structure to restore rich details of infrared cloud images. Chang et al. [31] adopt a residual multi-scale sub-network training method to construct a unified framework for correcting uniformity. This framework promotes the effective propagation of information through long-term and short-term residual learning mechanisms. Xu et al. [32] proposed a deep multi-scale densely connected convolutional neural network (DMD-CNN) to improve the correction performance by utilizing both fine and coarse features. Then, Chang et al. [49] adopted a U-shaped sampling network to fuse multi-scale and long-term and short-term residual information to correct image non-uniformity. Methods based on attention mechanism and adversarial generation are gradually introduced into image non-uniformity correction [33], [37]. Ding et al. [35] proposed a multi-scale residual network with attention mechanism to correct infrared non-uniformity, designed a multi-scale feature module to decompose the image, and used the channel space attention mechanism (CSAS) to extract deep features. Chen et al. [34] proposed a method for hyperspectral stripe restora-

tion, namely the Spatial Spectral Attention Pyramid Network (SAPN). This method adopts the Spatial Spectral Mixed Attention (SMA) mechanism to solve the problem of inefficient neighborhood representation in wide stripes. Yuan et al. [33] proposed a novel stripe removal method for infrared images, named Asymmetric Sampling Correction Network (ASCNet), which can effectively capture the global column-to-column relationship and integrate it into a U-shaped architecture. Wang et al. [36] proposed a model called Translution-SNet, which combines CNN with transformer technology to identify and extract key features between stripes and non-stripes. Yang et al. [37] proposed DestrCycleGAN, which uses prior stripe generation techniques to replace traditional auxiliary generators and corrects images by introducing gradient map reconstruction and cyclic consistency mechanism.

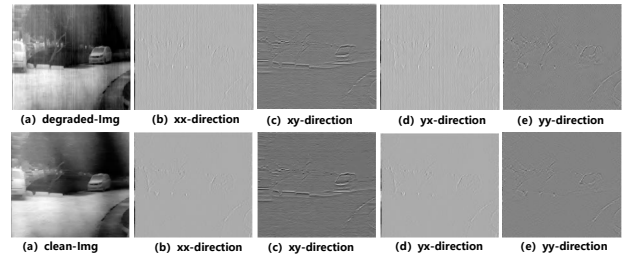


Fig. 5. Schematic diagram of the image patch similarity calculation and sorting process.

C. Optimization-based Non-uniformity Correction Method For Images

The optimization-based method sets a mathematical model based on the image characteristics to remove stripe noise [3], [25], [50]. Shen et al. used the prior likelihood probability density function to remove stripes and retain details [50]. Bouali et al. proposed a variational model based on the stripe direction characteristics [25]. Based on

this, Chang et al. proposed the ASSTV model to remove stripe noise using spectral spatial information [26]. However, since stripe noise is removed directly from the image, they often result in inaccurate stripe noise removal. Chen et al. [23] proposed a group sparsity-based model that exploits a difference-based constraint to describe the directional information of stripes. Wang et al. [51] proposed a new shear decomposition framework that uses unidirectional total variation to characterize the smoothness prior and removes diagonal stripes while retaining strong edges and geometric features. Based on the graph regularized low-rank representation technology, Lu et al. [52] proposed an innovative graph regularized low-rank representation de-striping method. Chang et al. [53] proposed a combined directional total variation and image-level low-rank prior to simultaneously adapt to different types of noise. Cao et al. [16] proposed a non-local total variation model that uses non-local region information of the image to remove stripe noise. KIM et al. [3] proposed the ADOM model. The model uses a weight-based detection strategy that can effectively identify and capture stripe noise components, and adopts an acceleration strategy based on the alternating direction multiplier method to achieve rapid removal of stripe noise.

III. PROPOSED METHOD

A. Preliminary Basic Definition

1) *Low-rank Approximation Theory*: By Eckart-Young-Mirsky matrix approximation theorem [54], low-rank matrix approximation aims to recover the underlying low-rank structure from degraded redundant observation data, where the degradation of the observation data is usually caused by noise interference. Assuming there is a matrix X with a low-rank structure and an observation matrix J eroded by noise E , the goal of low-rank approximation is to recover the underlying true structure \hat{X} without noise as accurately as possible given that J is known.

$$\arg \min_{\mathbf{X}} \|\mathbf{J} - \mathbf{X}\|_F^2, \quad \text{s.t. } \text{rank}(\mathbf{X}) \leq r, \mathbf{J} = \mathbf{X} + \mathbf{E} \quad (1)$$

In Eq 1, $\text{rank}(\mathbf{X})$ represents the rank of the matrix, and $\|\cdot\|_F$ represents the square of the Frobenius norm, that is, the sum of the absolute squares of the errors $\sum_{xy} |\mathbf{Y}_{xy} - \mathbf{X}_{xy}|^2$ between the observation matrix and the true data, which ensures that the $\hat{\mathbf{X}}$ can fit J more accurately. The self-similarity of infrared images in the degradation process may lead to data redundancy. When these redundant parts are used as observation matrices, they show low-rank characteristics [1].

2) *Singular Value Decomposition Theory*: We perform singular value decomposition (SVD) [55] on matrix J in Eq 1 using Eq 2.

$$J = U \Sigma V^T \quad (2)$$

In Eq 2, where $U = (u_1, \dots, u_n) \in R^{m \times n}$ and $V = (v_1, \dots, v_n) \in R^{n \times n}$ are matrices with orthogonal column

vectors, $U^T U = V^T V = I$. $\sum = \text{diag}(\sigma_1, \dots, \sigma_n)$ is a diagonal matrix, σ_i is a singular value, and $\sigma_1 \geq \sigma_2 \geq \dots \geq \sigma_n \geq 0$.

$$\hat{J} = U_k \Sigma_k V_k^T \quad (3)$$

More, by Eckart-Young-Mirsky matrix approximation theorem [54], for a matrix J of rank k , we aim to minimize the difference between J and \hat{J} while satisfying Eq 3 and 4. By retaining the first k largest singular values and setting the remaining singular values to zero, we are able to obtain the best low-rank approximation matrix J , $\|\cdot\|_F$ is the Frobenius norm.

$$\|J - \hat{J}\|_F^2 \geq \sum_{i=k+1}^n \sigma_i^2 \quad (4)$$

Therefore, the first k singular values retain most of the information, and the remaining small singular values can contribute negligibly to the overall structure [54].

B. The Proposed Framework

In this section, we propose a low-rank prior-based infrared non-uniformity image correction model. This model adopts a multi-stage denoising strategy to address various interference factors such as stripe noise, multiplicative noise, and mottled noise in non-uniform degraded images. This method aims to fully utilize the autocorrelation characteristics of infrared images and achieve non-uniformity correction by recovering potential low-rank structures from degraded redundant observation image.

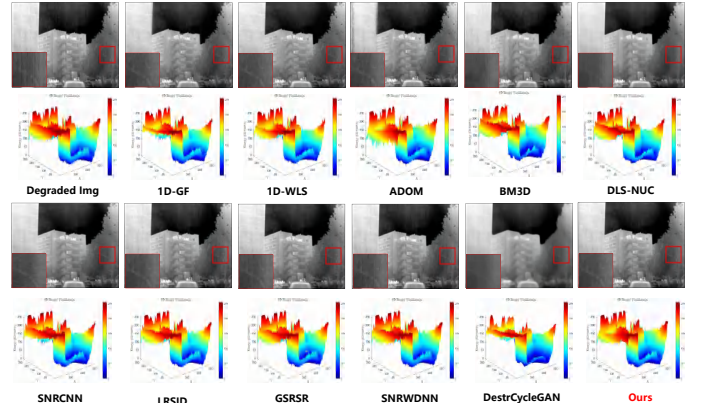


Fig. 6. Comparison of results of various methods and 3D representation of global energy in Yohann Dataset [56]. The red areas in the Fig represent zoomed-in details for detailed comparison.

C. Stage 1: Removing Stripe noise

Following references [3], [20] and [5], we define a stripe degradation model as Eq 5.

$$\mathcal{D}(x, y) = \mathcal{C}(x, y) + \mathcal{S}(x, y) + \mathcal{N}(x, y) \quad (5)$$

$\mathcal{D}(x, y)$ is the degraded image, $\mathcal{C}(x, y)$ is the restored image, $\mathcal{S}(x, y)$ is the stripe noise, and $\mathcal{N}(x, y)$ is the

environmental noise. x, y are the pixel positions of the image respectively.

In order to obtain $\mathcal{C}(x, y)$ from $\mathcal{D}(x, y)$, we set the optim objective function $\mathcal{E}(\cdot)$ in Eq 6. Among them, $\mathcal{F}(\cdot)$ is the fidelity term and $\mathcal{R}(\cdot)$ is the regularization term.

$$\mathcal{E}(D, C, S) = \mathcal{F}(D, C, S) + \mathcal{R}(C, S) \quad (6)$$

1) Data Fidelity Term: The fidelity term $\mathcal{F}(\cdot)$ is key to measuring the degree of image fitting, calculating the Euclidean distance between the restored image and the degraded image, and minimizing the fidelity term to make the restored image close to the undisturbed true image.

Ω represents the image domain.

$$\mathcal{F}(D, C, S) = \int_{\Omega} (\mathcal{D}(x, y) - (\mathcal{C}(x, y) + \mathcal{S}(x, y)))^2 dx \quad (7)$$

In Eq. 7, the introduction of the fidelity term $\mathcal{F}(\cdot)$ restores the image in the process of removing stripes, ensuring a high degree of consistency in semantic structure with the original image, otherwise it may lead to the loss or distortion of key structures during processing. Here, Ω represents the image domain.

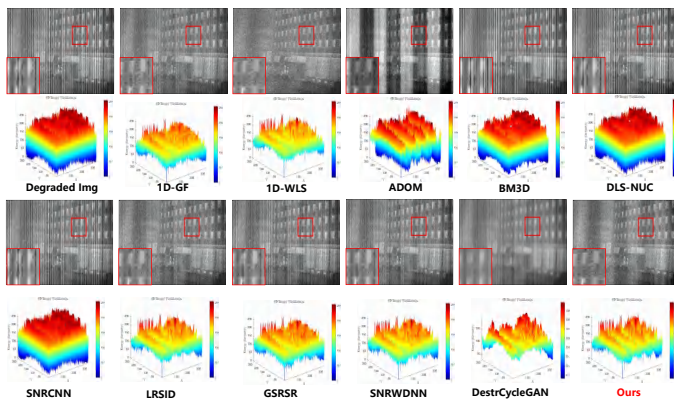


Fig. 7. Comparison of results of various methods and 3D representation of global energy in Yohann Dataset [56]. The red areas in the Fig represent zoomed-in details for detailed comparison.

2) Regularization Term: The SVD results of the stripe image are shown in Fig 3, indicating that the stripe noise has the characteristics of low-rank, the Schatten 1/2 norm can effectively approximate the rank of the matrix by minimizing the sum of the 1/2 powers of the singular values as Eq 8, providing a smoother optimization surface, thereby achieving effective control of stripe noise and accurate recovery of stripe components.

$$\mathcal{R}_1(S) = \left(\int_{\Omega} \sigma(S(x, y))^{1/2} dx dy \right)^2 \quad (8)$$

We can calculate the diagonal matrix $\sigma(\mathcal{S}(\cdot))$ of $\mathcal{S}(\cdot)$ using Eq 2.

Fig 1 and 2 show that infrared stripes mainly affect the horizontal gradient of the image. Regularization of the total variation promotes image smoothing by limiting the size of the gradient.

$$\mathcal{R}_2(C) = \int_{\Omega} |\nabla \mathcal{C}(x, y)| dx dy \quad (9)$$

Eq 9 can constrain the smoothness of the stripe direction, effectively reduce the horizontal gradient change, and alleviate the impact of stripes. $|\nabla \mathcal{C}(\cdot)|$ represents the gradient of $\mathcal{C}(\cdot)$ at the pixel (x, y) .

In Fig 5, the high-order gradients of the degraded image and the clean image in different directions are compared, showing that the stripes mainly damage the smoothness of the image in a specific direction.

$$\mathcal{R}_3(C) = \int_{\Omega} \left(\left| \frac{\partial^2 \mathcal{C}}{\partial x^2}(x, y) \right| \right) dx dy \quad (10)$$

Therefore, we use a high-order total variation constraint as in Eq 10 to ensure that the high-order smoothness of the image in the direction of the stripes is not damaged. So by Eq 6 , objective function $\mathcal{E}(\cdot)$ is rewritten as Eq 11.

$$\begin{aligned} & \mathcal{E}(D, C, S) \\ &= \frac{1}{2} \cdot \int_{\Omega} (\mathcal{D}(x, y) + \mathcal{C}(x, y) - \mathcal{S}(x, y))^2 dx dy \\ &+ \lambda_1 \left(\int_{\Omega} \sigma(\mathcal{S}(x, y))^{1/2} dx dy \right)^2 \\ &+ \lambda_2 \int_{\Omega} |\nabla \mathcal{C}(x, y)| dx \\ &+ \lambda_3 \int_{\Omega} \left(\left| \frac{\partial^2 \mathcal{C}}{\partial x^2}(x, y) \right| \right) dx dy \end{aligned} \quad (11)$$

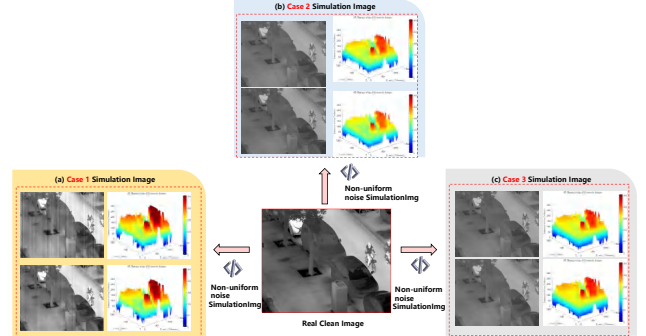


Fig. 8. The simulation results and 3D energy diagram of our proposed solution. Case 1 simulates conventional non-uniform noise, which is closer to the real scene. Case 2 is periodic uniform stripe noise, and case 3 is enhanced periodic uniform stripe noise, which is used to verify the potential performance of the methods.

3) Update and Convergence: Following [3], we use the ADMM algorithm [38] to divide Eq 11 into multiple subproblems for solution.

Firstly, we introduce auxiliary variables $\mathcal{Z}(\cdot)$, $\nabla \mathcal{C}'(\cdot)$ and $\mathcal{C}''(\cdot)$ in Eq 12 to enable the problem to be optimized by ADMM.

$$\begin{cases} \mathcal{Z}(x, y) = \sigma(S(x, y))^{1/2} \\ \nabla \mathcal{C}'(x, y) = \nabla \mathcal{C}(x, y) \\ \mathcal{C}''(x, y) = \frac{\partial^2 \mathcal{C}}{\partial x^2}(x, y) \end{cases} \quad (12)$$

Therefore, Eq 12 is rewritten as Eq 13.

$$\begin{aligned} \mathcal{E}(C, S, Z, \nabla C', C'') &= \frac{1}{2} \int_{\Omega} (D(x, y) + C(x, y) - S(x, y))^2 dx dy \\ &+ \lambda_1 \int_{\Omega} Z(x, y)^2 dx dy \\ &+ \lambda_2 \int_{\Omega} |\nabla C'(x, y)| dx dy \\ &+ \lambda_3 \int_{\Omega} |C''(x, y)| dx dy \end{aligned} \quad (13)$$

We construct the Lagrangian function, introduce the above constraints and add the corresponding Lagrangian multipliers $\lambda_Z(*)$, $\lambda'_C(*)$ and $\lambda''_C(*)$ to obtain Eq 14.

$$\begin{aligned} L(C, S, Z, \nabla C', C'', \lambda_Z, \lambda'_C, \lambda''_C) &= E(C, S, Z, \nabla C', C'') \\ &+ \int_{\Omega} \lambda_Z(x, y) (Z(x, y) - \sigma(S(x, y))^{1/2}) dx dy \\ &+ \int_{\Omega} \lambda'_C(x, y) (\nabla C'(x, y) - \nabla C(x, y)) dx dy \\ &+ \int_{\Omega} \lambda''_C(x, y) \left(C''(x, y) - \frac{\partial^2 C}{\partial x^2} \right) dx dy \end{aligned} \quad (14)$$

Update $C(*)$. Fix $S(*)$, $Z(*)$, $\nabla C'(*)$ and $C''(*)$, optimize $C(*)$ by Eq 15. Eq 15 describes a standard image restoration problem, which we solve by gradient descent [57].

$$\begin{aligned} \mathcal{C}^{k+1} &= \arg \min_C \left\{ \frac{1}{2} \int_{\Omega} (D(x, y) + C(x, y) - S(x, y))^2 dx dy \right. \\ &\quad \left. + \lambda_2 \int_{\Omega} |\nabla C'(x, y)| dx dy + \lambda_3 \int_{\Omega} |C''(x, y)| dx dy \right\} \end{aligned} \quad (15)$$

Update $S(*)$. Fix $C(*)$, $Z(*)$, $\nabla C'(*)$ and $C''(*)$, optimize $S(*)$ by Eq 16. This subproblem in Eq 15 can be described as a least squares model and solved using gradient descent.

$$\begin{aligned} \mathcal{S}^{k+1} &= \arg \min_S \left\{ \frac{1}{2} \int_{\Omega} (D(x, y) + C(x, y) - S(x, y))^2 dx dy \right. \\ &\quad \left. + \lambda_1 \int_{\Omega} Z(x, y)^2 dx dy \right\} \end{aligned} \quad (16)$$

Update $Z(*)$. Fix $C(*)$, $S(*)$, $\nabla C'(*)$ and $C''(*)$, optimize $Z(*)$ by Eq 17. We use the iterative shrinkage thresholding algorithm (ISTA) [58] to solve Eq 17.

$$\mathcal{Z}^{k+1} = \arg \min_Z \left\{ \lambda_1 \int_{\Omega} Z(x, y)^2 dx dy \right\} \quad (17)$$

Update $\nabla C'(*)$. Fix $C(*)$, $S(*)$, $Z(*)$ and $C''(*)$, optimize $\nabla C'(*)$ by Eq 18. We use ISTA to solve.

$$\nabla C'^{k+1} = \arg \min_{\nabla C'} \left\{ \lambda_2 \int_{\Omega} |\nabla C'(x, y)| dx dy \right\} \quad (18)$$

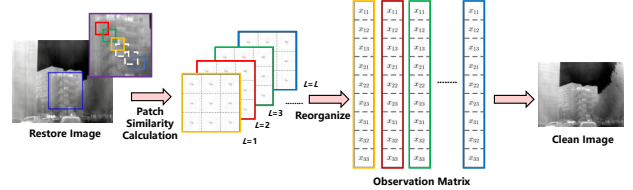


Fig. 9. Schematic diagram of the observation matrix construction process.

Update $C''(*)$. Fix $C(*)$, $S(*)$, $Z(*)$ and $\nabla C'(*)$, optimize $C''(*)$ by Eq 19. We use ISTA to solve.

$$C''^{k+1} = \arg \min_{C''} \left\{ \lambda_3 \int_{\Omega} |C''(x, y)| dx dy \right\} \quad (19)$$

Update Lagrange multipliers. After each iterative calculation of each subproblem, the corresponding Lagrange multiplier λ_Z^{k+1} , λ'_C^{k+1} and λ''_C^{k+1} need to be updated. Among them, ρ is the penalty factor that controls the step size of the update. In Eq 20, the difference between the k -th and $k+1$ -th iterations is calculated in each iteration to adjust the multiplier.

$$\begin{cases} \lambda_Z^{k+1} = \lambda_Z^k + \rho (Z^{k+1}(x, y) - \sigma(S^{k+1}(x, y))^{1/2}) \\ \lambda'_C^{k+1} = \lambda'_C^k + \rho (\nabla C'^{k+1}(x, y) - \nabla C^{k+1}(x, y)) \\ \lambda''_C^{k+1} = \lambda''_C^k + \rho \left(C''^{k+1}(x, y) - \frac{\partial^2 C(x, y)}{\partial x^2} \right) \end{cases} \quad (20)$$

Convergence Criteria.

We use Eq 21 to make convergence judgment. ϵ is the threshold and k is the maximum number of iterations, $\|\cdot\|_F$ represents the Frobenius norm. $\mathcal{C}^k(*)$ is the restored image of the k -th iteration, and $\mathcal{C}^{k+1}(*)$ is the restored image obtained after the $k+1$ -th iteration.

$$\frac{\|\mathcal{C}^{k+1}(x, y) - \mathcal{C}^k(x, y)\|_F}{\|\mathcal{C}^k(x, y)\|_F} > \epsilon \text{ And } k < \text{maxiter} \quad (21)$$

Whether the model has converged is determined by measuring the relative change between the results of two adjacent iterations. The smaller the relative change, the closer the algorithm is to convergence.

D. Stage 2: Removing environment noise

According to Eq 1, the key step of using a low-rank matrix to approximate a model is to construct an observation matrix, that is, the observation matrix must have a potential low-rank structure.

For specific restored image $\mathcal{C}(x, y)$, it is first divided into M overlapping equal-sized image patches, each with size of 11×11 . Then, each of these image patches is selected one by one as a reference patch, and the first image patch \mathcal{C}_0 is selected as the reference image patch in Fig 10.

$$\mathcal{H}(y_j, y_c) = \int_{\Omega} (y_j(x, y) - y_c(x, y))^2 dx \quad (22)$$

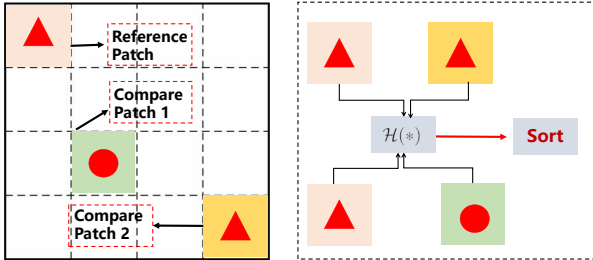


Fig. 10. Schematic diagram of the image patch similarity calculation and sorting process.

This similarity measure reflects the difference in pixel values between two patches. The smaller the difference, the higher the similarity. When calculating, for each pixel position, take the sum of the squares of the pixel value differences between the reference patch and the candidate patches to obtain the similarity measure \mathcal{H} .

We sort by similarity measure and select the smallest first L image patches for reorganization to form the new observation matrix \mathcal{G} of Eq 23.

$$\mathcal{G} = [\mathbf{y}_j, \mathbf{y}_{(c,1)}, \dots, \mathbf{y}_{(c,L)}]. \quad (23)$$

In Fig 9, using the blue patch as a benchmark, find similar patches in the image and stack them. There is significant redundancy within stacked image patches. Therefore, these two-dimensional image similarity patches can be expanded and used as column vectors of the matrix in turn to form the required observation matrix \mathcal{G} .

Inspired by Eq 1, we give the conditional relationship between the observation matrix \mathcal{G} and its estimation matrix $\hat{\mathcal{G}}$. τ is the standard deviation of the noise, which indicates the strength of the noise, $\|\cdot\|_F$ represents the Frobenius norm in Eq 24.

$$\arg \min_{\mathcal{G}} \|\mathcal{G} - \hat{\mathcal{G}}\|_F^2 = \tau^2 \quad (24)$$

According to the low-rank matrix approximation principle [54], we rewrite Eq 24 into Eq 25. \mathcal{G}_k can remove the noise represented by smaller singular values while retaining the main structural information of the image (represented by the singular vectors corresponding to larger singular values).

$$\arg \min_{\mathcal{G}} \|\mathcal{G}_k - \hat{\mathcal{G}}\|_F^2 = \tau^2 \quad (25)$$

In Eq 26, the value of parameter k , is related to the size of variable τ and singular values. If the sum of the squares of the $k + 1$ -th to the last singular value is less than τ^2 , then the selected a value is appropriate. This criterion indicates that selecting the first few singular values can eliminate noise and retain enough information to estimate the matrix \mathcal{G} . Therefore, the k can automatically adjust the number of singular values retained and effectively remove noise.

$$\sum_{i=k}^n \sigma_i^2 > \tau^2 \geq \sum_{i=k+1}^n \sigma_i^2 \quad (26)$$

After obtaining the estimated matrix through the above equation, the clean image is reconstructed by back projection.

TABLE I
QUANTITATIVE EVALUATION OF DIFFERENT METHODS ON REAL AND SIMULATED IMAGES. THE HIGHEST AND SECOND-HIGHEST SCORES ARE INDICATED IN **BOLD** AND UNDERLINE RESPECTIVELY.

Data	Metrics	ID-GF	ID-WLS	ADOM	BM3D	DLS-NUC	SNRCCN	LRSID	GSRSH	SNRWDDNN	DestCycleGAN	Ours
Img1	AVGE	0.0056	0.1578	0.0654	0.2574	1.3321	2.3140	0.0441	0.0047	0.1547	6.5412	0.0021
	MRD	0.1941	0.1704	1.5415	2.0145	0.2955	0.1647	0.0547	0.0742	0.5442	1.0014	0.0354
	AAD	3.9211	3.3841	2.1476	5.6615	3.1249	8.5110	1.6654	13.492	4.6504	9.5474	<u>1.7882</u>
	ICV	43.1172	40.3256	47.9855	45.7456	48.6540	50.3367	56.7458	58.1472	56.4474	55.6471	<u>57.1474</u>
Img2	ρ	0.5048	0.4872	0.4123	0.4412	0.4126	0.4925	0.3995	0.39547	0.3746	0.5122	0.3611
	AVGE	4.0103	4.3231	6.2145	4.6002	5.9847	7.0661	2.3148	8.8654	2.0446	2.3660	1.5418
	MRD	0.6688	0.7619	3.6743	2.5614	0.0314	1.6322	0.1090	0.6409	1.4475	1.2474	0.0285
	AAD	3.5563	3.3680	3.1987	2.9741	2.8651	2.6576	2.3120	2.5528	2.4369	2.5621	<u>2.3690</u>
Img3	ICV	68.1208	66.5562	60.654	69.5416	66.4099	69.7123	<u>73.1541</u>	71.6548	72.5469	69.1245	73.6654
	ρ	0.5740	0.5862	0.6211	0.6254	0.6123	0.6315	0.5416	0.5614	0.5678	0.5771	<u>0.5588</u>
	AVGE	0.6543	0.1671	1.2378	2.0456	1.1650	0.2604	0.0038	0.0109	0.0844	0.0321	0.0005
	MRD	0.7490	0.8525	4.160	2.8684	5.7172	1.8267	0.1897	0.0351	1.6196	1.3969	0.0319
Img4	AAD	4.3897	3.8662	3.6785	3.4202	3.2969	3.0502	<u>2.7183</u>	2.9357	2.8034	2.9464	2.6598
	ICV	45.5254	47.2263	50.1274	49.6633	<u>55.3967</u>	53.9655	54.6621	52.6683	54.3271	49.3504	55.3203
	ρ	0.4306	0.4155	0.4160	0.4005	0.4321	0.4412	0.3987	0.3865	0.4233	0.4245	0.3874
	AVGE	0.7721	1.4600	0.1972	1.5747	2.4112	0.3073	0.6128	0.0105	0.0995	0.0379	0.0041
Img5	MRD	0.2114	0.1850	2.1948	1.6814	0.3224	0.1793	0.0597	0.0869	0.5930	1.3915	<u>0.0686</u>
	AAD	4.2596	3.7488	3.5660	3.3178	3.1985	2.9607	2.6384	<u>2.5866</u>	2.7173	2.8610	<u>2.8530</u>
	ICV	41.8812	43.4293	46.1115	45.6633	50.0395	49.6932	50.3088	48.4243	49.9261	45.4424	50.9028
	ρ	0.5224	0.5353	0.5652	0.5291	0.5563	0.5707	0.4911	0.5318	0.5163	0.5259	0.4874
Img6	AVGE	0.8364	1.6202	0.2196	1.3499	2.8784	0.3411	0.0111	0.6795	0.1104	0.0420	0.0046
	MRD	0.7125	0.8256	3.9866	2.7530	0.0343	1.7376	0.1840	0.0945	1.5609	1.3472	0.0311
	AAD	4.6179	4.0803	3.8841	3.5983	3.4817	3.2215	2.8685	2.8159	2.9354	3.1104	<u>3.1022</u>
	ICV	46.5588	48.3621	51.2928	50.8093	56.3192	56.3284	55.8603	53.8610	55.4524	50.4971	56.5987
Img7	ρ	0.6142	0.4884	0.4493	0.4325	0.4267	0.4761	0.4306	0.4673	0.4584	0.4360	0.4186
	AVGE	1.1133	2.1366	0.6915	2.2340	3.4793	0.4654	0.8845	0.0652	0.1435	0.0546	<u>0.0069</u>
	MRD	0.2338	0.2081	2.4847	1.8901	0.3581	0.1987	0.0666	0.0787	0.0784	1.5373	<u>0.0987</u>
	AAD	4.1948	3.6872	2.3180	6.2277	3.3741	9.2760	<u>1.9830</u>	14.7494	5.0719	10.2948	1.9123
Img8	ICV	51.4934	54.3424	58.1781	56.6413	62.7542	63.4673	61.7744	60.5249	61.2986	57.2769	62.8384
	ρ	0.4806	0.4682	0.4673	0.4528	0.4435	0.4969	0.4473	0.4835	0.4765	0.4794	<u>0.4353</u>

IV. EXPERIMENTS

A. Dataset And Evaluation Metrics

1) Dataset: We conducted experiments on two challenging public datasets and simulation datasets.

Real Dataset: Yohann et al. proposed an online correction method and created a website aimed at collecting infrared non-uniformity images uploaded by other researchers [56]. Specifically, Yohann et al. contributed 21 infrared images covering various scenes such as parking lots, buildings, roads, flowers, and schools. In addition, there are 30 images provided by other researchers, which include various application scenarios such as portraits, vehicles, pedestrians, and indoor objects. The DLS-NUC dataset was proposed by He et al [47]. with the aim of applying it to non-uniformity correction in the field of deep learning. This dataset contains 100 clean images used to simulate the generation of non-uniform images, as well as 22 degraded infrared non-uniform images, all with a resolution of 640×480 pixels. Its scenarios mainly cover outdoor vehicles, buildings, and indoor objects.

Simulation Dataset: Real datasets can accurately reflect the performance of algorithms in real application environments, but their generalization ability is relatively limited. In contrast, simulated datasets can deeply explore the potential correction performance of various methods, and the scene settings are more flexible and varied. Therefore, we proposed a simulated dataset, which generates simulated degraded images by introducing non-uniform noise of different intensities into clean infrared images. We propose to use generally recognized, authentic and uncontaminated infrared images such as LLVIP [59] and TNO [60] to simulate the generation of degraded images.

In Fig 8, we precisely control the amplitude and frequency of stripes and white noise, and obtain two types of non-uniform images.

The collected infrared non-uniform images and simulation code can be obtained through this link: [IR-non-uniformity](#), and we will continue to work on maintaining and expanding the non-uniform response images.

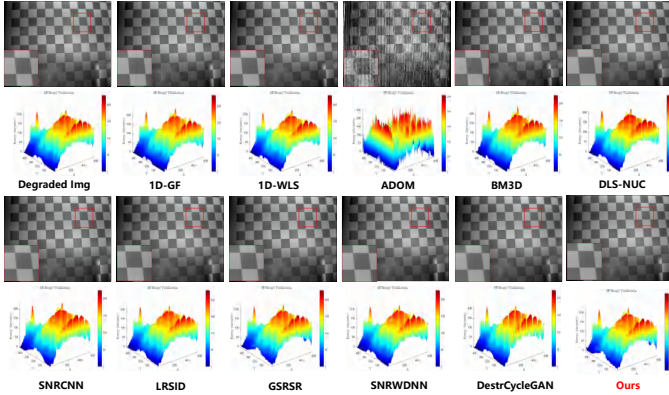


Fig. 11. Comparison of results of various methods and 3D representation of global energy in He Dataset [47]. The red areas in the Fig represent zoomed-in details for detailed comparison.

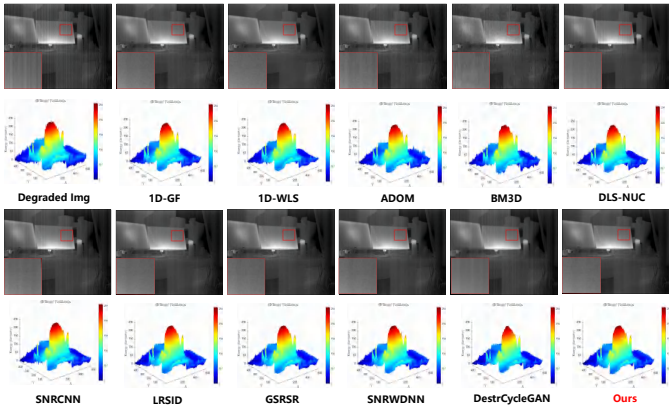


Fig. 12. Comparison of results of various methods and 3D representation of global energy in He Dataset [47]. The red areas in the Fig represent zoomed-in details for detailed comparison.

2) Evaluation Metrics:

We use seven metrics to comprehensively evaluate the image results, including peak signal-to-noise ratio (PSNR [61]), structural similarity index (SSIM [62]), average vertical gradient error (AVGE) [63], image roughness index (ρ) [64], average absolute difference (AAD) [46], inverse coefficient of variation (ICV) [3], [65] and mean relative deviation (MRD) [3], aiming to achieve quantitative analysis and comprehensive evaluation of image quality. Due to space limitations, we will not elaborate on PSNR, and SSIM, but you can refer to the original references [61], [62], [66], for more information. We have rewritten the code for all quantitative evaluation metrics. The code and resources can be found at [Image-Quality](#) and [InfraredISP-Quality](#).

AVGE measures the algorithm's ability to preserve image details by comparing the difference in vertical gradients between the original image and the processed image.

$$\text{AVGE} = \frac{1}{N} \sum_{N=1}^N \left\| \nabla_y \hat{f}(x, y) - \nabla_y f(x, y) \right\| \quad (27)$$

In Eq 27, N is the total number of pixels, ∇_y is the vertical gradient operator, and $f(x, y)$ and $\hat{f}(x, y)$ are the pixels before and after processing, respectively. The closer the AVGE value is to 0, it indicates that the method retains more semantic detail information while removing non-uniform noise.

ρ evaluates the richness of image details and texture. Calculating the ρ value of the original and processed images can quantitatively analyze the ability to retain details. The lower the ρ value, the lower the non-uniformity in Eq 28.

$$\rho(f) = \frac{\|h * f(x, y)\| + \|h^T * f(x, y)\|}{\|f(x, y)\|} \quad (28)$$

Here, h represents a differential filter used for extracting edge or texture features, $*$ denotes the convolution operation, which applies the filter to the original image $f(x, y)$, and $\|\cdot\|$ represents the first-order norm, commonly used to measure the energy or magnitude of the filtered image.

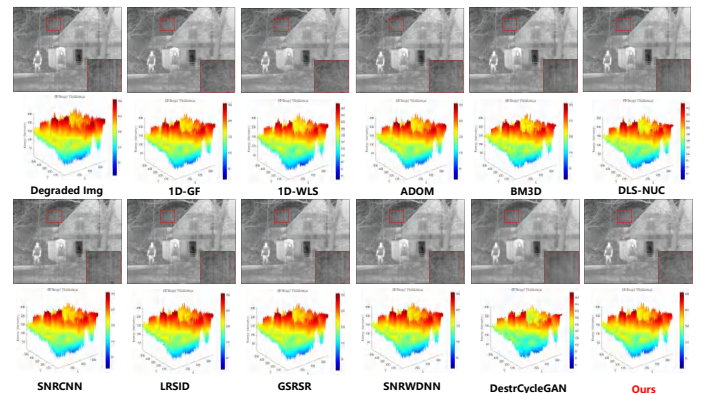


Fig. 13. Using the TNO [60] dataset as a simulated degradation image, the results of various methods are compared, and the 3D diagram of the global energy is shown. The red area in the figure represents the enlarged details for detailed comparison.

ICV is commonly used to evaluate the smoothing and de-uniformization effects of images in Eq 29. μ and σ represent the pixel mean and standard deviation of the selected area in the image, respectively.

$$\text{ICV} = \frac{\mu}{\sigma} \quad (29)$$

In addition, the value of ICV is positively correlated with the smoothness of the image.

AAD quantifies the mean absolute difference between the output image and the original noise-free image, which is used to measure the difference between the two images.

$$\text{AAD} = \frac{1}{m \times n} \sum_{i=1}^m \sum_{j=1}^n |\hat{f}(x, y) - f(x, y)| \quad (30)$$

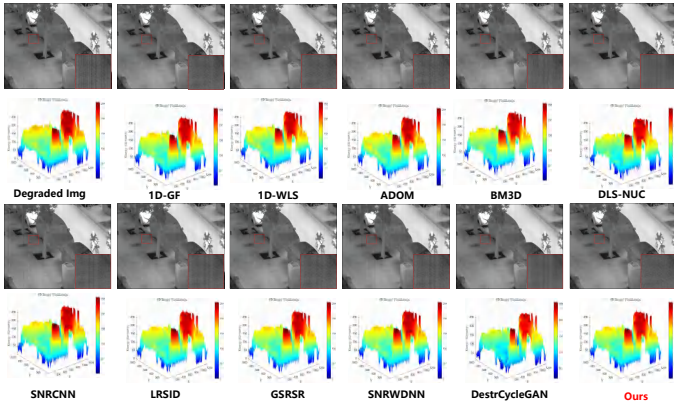


Fig. 14. Using the LLVIP dataset as a simulated degradation image, the results of various methods are compared, and the 3D diagram of the global energy is shown. The red area in the figure represents the enlarged details for detailed comparison.

In Eq 30 is used to measure the difference between the processed image $\hat{f}(x, y)$ and the original image $f(x, y)$, m and n are the height and width of the $f(x, y)$ or $\hat{f}(x, y)$.

$$\text{MRD} = \frac{1}{m \times n} \sum_{i=1}^m \sum_{j=1}^n \left| \frac{\hat{f}(x, y) - f(x, y)}{f(x, y)} \right| \quad (31)$$

MRD in Eq 31 is used to measure the difference between the processed image $\hat{f}(x, y)$ and the original image $f(x, y)$, m and n are the height and width of the $f(x, y)$ or $\hat{f}(x, y)$. The smaller the MRD value, the smaller the relative deviation between the $\hat{f}(x, y)$ and the $f(x, y)$.

B. Comparison Methods And Experimental Parameters

We conducted a comparative analysis of existing stripe removal methods, including 1D-GF [19], 1D-WLS [67], BM3D [68], DLS-NUC [47], LRSID [24], SNRCNN [29], GSRSR [23], SNRWDNN [69], ADOM [3] and DestrCycleGAN [37], to verify the potential performance of methods. The original parameters of all methods can be verified in the provided paper and code, and we strictly followed the optimal parameter configuration set by the original author during the experimental process. We set the maximum number of iterations k for Eq 21 to 250, and the relative error threshold ϵ to 1e-5. Set L to 50 in Eq 23. λ_1 , λ_2 and λ_3 are both set to 1e-3 in Eq 13. All experiments on our method were performed on a PC with a Core (TM) i9-11900 @ 2.50GH, RTX 3060 and 64G RAM with Matlab 2024a.

C. Experimental Results And Analysis

We perform experiments on four real degraded images and two simulated degraded images to evaluate the potential effectiveness of the exit methods. It is worth noting that most ablation experiments are performed on real degraded images. In addition, degraded images generated by applying non-uniform noise of different intensities are used to further explore the performance limit of the method. The highest and second-highest scores are indicated in **bold** and underline respectively.

1) Qualitative Evaluation: Fig 6 to Fig 14, we present the visualization results of different methods, as well as detailed magnification images and corresponding 3D energy maps. The energy map can magnify subtle differences, making it easier to compare the correction effects of different methods. Except for Fig 2, most methods show consistent results trends. This is because the non-uniform noise in most scenes is relatively weak, allowing various methods to fully exert their performance advantages. In particular, DestrCycleGAN adopts an adversarial generative network architecture, and it can be observed from the detailed magnification that the gradient information is not preserved. The results of filter-based methods, such as 1D-GF, 1D-WLS, and BM3D, are similar to those of DestrCycleGAN, especially in terms of retaining texture information. However, while removing environmental

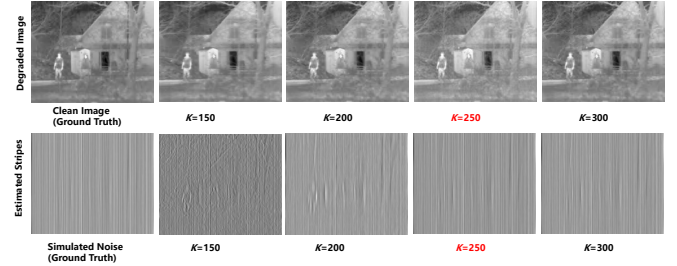


Fig. 15. Visualization of the results at different iterations. Qualitative evaluation is performed by comparing the stripe noise and the restored image.

noise, filtering-based methods also lead to a certain degree of loss of image structure. Results obtained using optimization-based methods are often able to produce images consistent with human visual perception. However, in Fig 11, ADOM destroys the information structure of the original image during processing. It is particularly worth noting that the image presented in Fig 7 has significant non-uniformity, which provides sufficient challenges for testing the noise correction capabilities of the algorithm. Unfortunately, none of the tested methods completely eliminated the noise. ADOM, BM3D, and DLS-NUC methods even produce inferior results than the original degraded images. In contrast, the images obtained through our proposed pipeline are able to maintain a certain degree of image recovery capability. Last, Fig 13 and Fig 14 show the experimental results on the simulation images. The method proposed in this study successfully obtained clear infrared images, and it was observed that the image sharpness was well maintained in the detail amplification area, with significant gradient information. In contrast, images obtained by other methods lack detailed textures.

2) Quantitative Evaluation: In Table I, by the quantitative evaluation comparison of the six scenarios shown in Fig 6 to Fig 14, it is proved that the proposed method shows significant performance advantages in multiple scenarios. This result not only verifies the ability of this research in image detail processing and can maximize the preservation of texture richness, but also highlights the advantages of this research algorithm in low-rank estimation. Combining

high-order directional characteristics and low-rank models, effectively eliminates stripe noise. Furthermore, our NUC pipeline demonstrates excellent performance, ensuring accurate image reconstruction and detail preservation by multi-stage optimization. Filter-based method is unstable in terms of result scores, as the uncertainty of non-uniform noise leads to inconsistent loss of image details, which causes unstable quantitative evaluation scores. The optimization-based method uses image prior information to construct the objective function, and has better evaluation score performance. This may be because learning-based methods rely on a large amount of real data for supervised training, and due to the lack of paired datasets, the obtained models are insufficient in generalization ability.

3) Ablation Experiment: In this section, we will use simulated images for analysis, as simulated images can provide images before degradation as ground truth, which will be helpful for comparison.

Maximum number of iterations. The setting of the maximum number of iterations ensures that the algorithm has enough iterations to find a better solution, while also avoiding the waste of computing resources and time consumption caused by too many iterations. Fig 15 shows the visualization results of different numbers of iterations on degraded images. In Fig 15, the stripe noise is effectively estimated when the k value reaches 250. However, when the k value is 150 and 200, the original semantic information of the image is mistakenly judged as noise and removed.

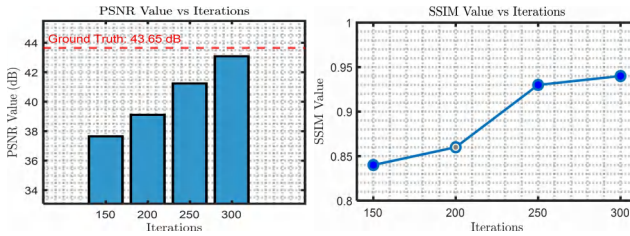


Fig. 16. Quantitative evaluation graphs for different iteration numbers. The left is the PSNR figure, and the right is the SSIM figure.

When the number of iterations reaches 250, both the quantitative evaluation indicators PSNR and SSIM can maintain high value. However, when the number of iterations is set to 300, although the index is slightly improved, the time cost required for solution increases significantly. In addition, the obtained visualization results maintain a high consistency with the iteration number of 250.

Experiments with different non-uniform noise intensities. We performed non-uniform noise stress experiments on simulated images to evaluate the potential performance of our pipeline under different response modes. While maintaining the environmental noise level constant, stripe noise intensity is gradually introduced in Fig 17. Experimental results show that our proposed method can still achieve satisfactory results and demonstrate significant robustness in the face of high-intensity

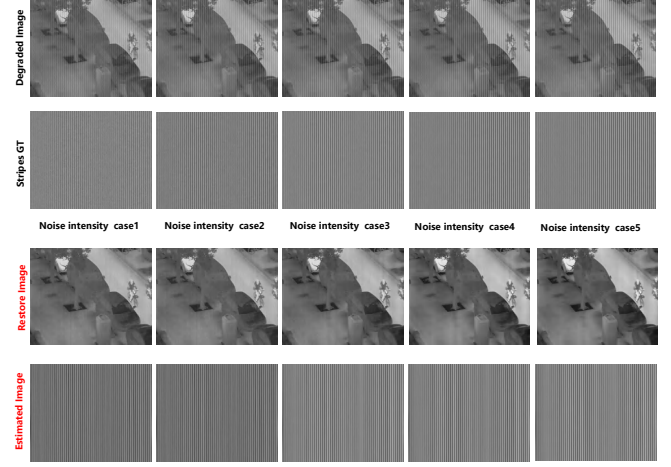


Fig. 17. Ablation experiments under different stripe noise intensities. The vertical stripe intensity increases from case 1 to case 5. **For the most complete experience, please zoom in on this image on the screen.**

TABLE II
THE AVERAGE RUNNING TIME OF DIFFERENT METHODS ON DIFFERENT DATASETS. UNIT (SECONDS)

Methods	Yohann [56]	DLS-NUC-Data [47]	Simu w/ TNO [60]	Simu w/ M3FD [70]	Simu w/ LLVIP [59]	Simu w/ MSRS [71]
1D-GF [19]	1.66	2.47	1.88	2.23	3.12	1.89
1D-WLS [67]	1.84	1.96	2.05	2.71	4.12	2.56
ADM [30]	8.50	10.44	9.13	11.4	12.58	10.87
BMDL [68]	10.33	11.23	13.65	12.78	18.65	13.67
DLS-NUC [47]	4.62	4.25	6.09	6.34	7.89	6.77
SNR [29]	5.68	5.57	6.58	6.60	8.15	7.46
LRSID [24]	7.03	6.76	7.16	7.31	9.68	8.83
GSRSR [23]	7.48	7.28	7.55	8.43	10.36	8.67
SNR-GAN [69]	5.84	6.12	6.86	7.01	8.84	7.22
DestrCycleGAN [37]	4.89	5.20	6.09	6.88	6.63	5.67
Ours	6.51	7.14	6.22	6.86	10.36	7.84

non-uniform noise interference. This is due to the fact that we consider the low-rank and directional characteristics when estimating the stripe noise.

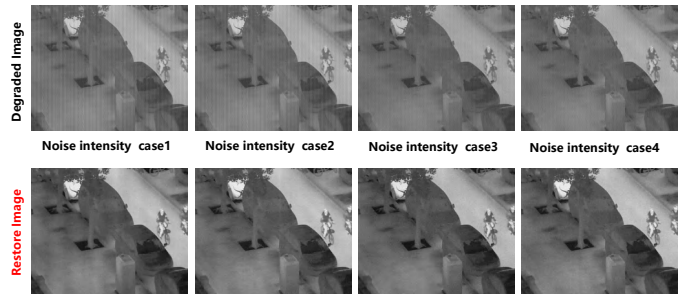


Fig. 18. Schematic diagram of image restoration results under different numbers of patches. The vertical environment noise intensity increases from case 1 to case 4. **For the most complete experience, please zoom in on this image on the screen.**

In Fig 18, we maintain the intensity of the stripe noise unchanged while introducing low-frequency ambient noise. Since our multi-stage single-frame NUC process takes into account the low-rank characteristics of ambient noise, it can effectively remove the ambient noise while removing the stripe noise, thereby obtaining a high-quality restored image.

Experimental verification of the optimal L value for the observation matrix. Fig 20 presents the image restoration results obtained by applying observation matrices constructed with different numbers of matrix patches. In the first row, it is evident that without im-

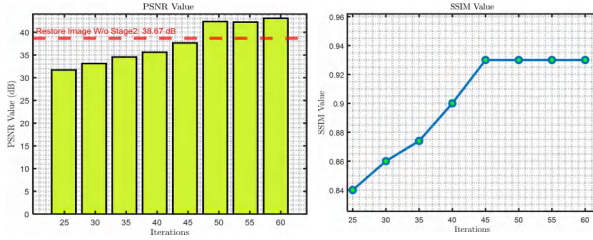


Fig. 19. Quantitative evaluation figure for different numbers of patches. The left is the PSNR figure, and the right is the SSIM figure. **For the most complete experience, please zoom in on this image on the screen.**

plementing the second stage of low-rank matrix approximation to exclude environmental noise, there is significant noise interference in the resulting image. The second and third rows show the comparative effects of different numbers of matrix patches. It can be observed from the second row of images that the image loses obvious gradient information due to the use of a smaller number of matrix patches for estimation. When the number of matrix patches L reaches 50, the denoising effect can be effectively maintained from the observation matrix, and the texture details can be obviously preserved. However, further increasing the number of matrix blocks does not significantly improve the image quality, but instead causes the optimization process to consume more time. The PSNR and SSIM of Fig 19 validate the effectiveness of the quantitative evaluation.

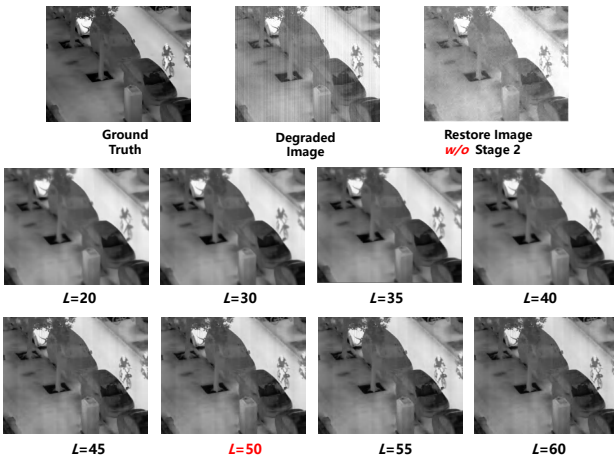


Fig. 20. Schematic diagram of image restoration results under different patches. **For the most complete experience, please zoom in on this image on the screen.**

4) Run Time Analysis: Based on the experimental parameter settings above, we compared the running time of different methods. The running time test comparison results of different methods in Table II. We use the case 2 stripe simulation scheme in Fig 8 to test the LLVIP [59], M3FD [70], TNO [60], and MSRS [71] datasets to evaluate the time efficiency potential of each method under different resolutions and scenarios. Each dataset is tested 20 times, with 10 repetitions each time, and the average is taken to exclude accidental errors. Table II shows that the

filtering-based method has the shortest processing time in image processing, the optimization method takes the longest time, and the learning-based method uses the GPU to reduce time consumption. Our work has moderate performance in real and simulated degraded image tests, but is better than the optimization-based method in time efficiency.

V. CONCLUSIONS

In this paper, we design a pipeline for correcting the non-uniformity of single-frame infrared images, which uses various prior information of the image to estimate the clear image from the degraded image. Specifically, we use the high-order directionality and low-rank characteristics of the streak image to design a diagonal nuclear norm and high-order gradient variational optimization model to remove the stripes image, and use the ADMM algorithm to solve the sub-problems. In addition, we take the environmental noise into consideration and use the low-rank matrix approximation theory to obtain a clean image. Extensive experiments demonstrate the superiority of our method. In the future, we will design an acceleration strategy for the ADMM algorithm to improve the running speed of the algorithm, and propose simulation images of multiple scenes to provide data support for subsequent research.

REFERENCES

- [1] L. Cai, X. Dong, K. Zhou, and X. Cao, “Exploring video denoising in thermal infrared imaging: Physics-inspired noise generator, dataset and model,” *IEEE Transactions on Image Processing*, 2024.
- [2] C. Lu, “Stripe non-uniformity correction of infrared images using parameter estimation,” *Infrared Physics & Technology*, vol. 107, p. 103313, 2020.
- [3] N. Kim, S.-S. Han, and C.-S. Jeong, “ADOM: ADMM-based optimization model for stripe noise removal in remote sensing image,” *IEEE Access*, vol. 11, pp. 106587–106606, 2023.
- [4] Z. Wu and X. Wang, “Non-uniformity correction for medium wave infrared focal plane array-based compressive imaging,” *Optics Express*, vol. 28, no. 6, pp. 8541–8559, 2020.
- [5] L. Lei, D. Song, P. He, and H. Lin, “Strip noise removal of infrared images acquired by trackside based on noise adaptive modification,” *IEEE Sensors Journal*, 2024.
- [6] L. Song and H. Huang, “Spatial and temporal adaptive nonuniformity correction for infrared focal plane arrays,” *Optics Express*, vol. 30, no. 25, pp. 44 681–44 700, 2022.
- [7] X. Ying, C. Xiao, R. Li, X. He, B. Li, Z. Li, Y. Wang, M. Hu, Q. Xu, Z. Lin *et al.*, “Visible-thermal tiny object detection: A benchmark dataset and baselines,” *arXiv preprint arXiv:2406.14482*, 2024.
- [8] Z. Küttük and G. Algan, “Semantic segmentation for thermal images: A comparative survey,” in *Proceedings of the IEEE/CVF Conference on Computer Vision and Pattern Recognition*, 2022, pp. 286–295.
- [9] C. Guo, C. Liu, L. Deng, Z. Chen, M. Dong, L. Zhu, H. Chen, and X. Lu, “Multi-scale infrared and visible image fusion framework based on dual partial differential equations,” *Infrared Physics & Technology*, vol. 135, p. 104956, 2023.
- [10] C. Liu, H. Chen, L. Deng, C. Guo, X. Lu, H. Yu, L. Zhu, and M. Dong, “Modality specific infrared and visible image fusion based on multi-scale rich feature representation under low-light environment,” *Infrared Physics & Technology*, vol. 140, p. 105351, 2024.
- [11] H. Chen, L. Deng, Z. Chen, C. Liu, L. Zhu, M. Dong, X. Lu, and C. Guo, “Sfcfusion: Spatial-frequency collaborative infrared and visible image fusion,” *IEEE Transactions on Instrumentation and Measurement*, 2024.

- [12] C. Liu, X. Sui, Y. Liu, X. Kuang, G. Gu *et al.*, “Fpn estimation based nonuniformity correction for infrared imaging system,” *Infrared Physics & Technology*, vol. 96, pp. 22–29, 2019.
- [13] J. G. Harris and Y.-M. Chiang, “Nonuniformity correction of infrared image sequences using the constant-statistics constraint,” *IEEE Transactions on image processing*, vol. 8, no. 8, pp. 1148–1151, 1999.
- [14] B. Narayanan, R. C. Hardie, and R. A. Muse, “Scene-based nonuniformity correction technique that exploits knowledge of the focal-plane array readout architecture,” *Applied optics*, vol. 44, no. 17, pp. 3482–3491, 2005.
- [15] W. Zhao and C. Zhang, “Scene-based nonuniformity correction and enhancement: pixel statistics and subpixel motion,” *JOSA A*, vol. 25, no. 7, pp. 1668–1681, 2008.
- [16] W. Cao, Y. Chang, G. Han, and J. Li, “Destriping remote sensing image via low-rank approximation and nonlocal total variation,” *IEEE Geoscience and Remote Sensing Letters*, vol. 15, no. 6, pp. 848–852, 2018.
- [17] P. Rakwatin, W. Takeuchi, and Y. Yasuoka, “Restoration of aqua modis band 6 using histogram matching and local least squares fitting,” *IEEE Transactions on Geoscience and Remote Sensing*, vol. 47, no. 2, pp. 613–627, 2008.
- [18] Y. Tendero, S. Landeau, and J. Gilles, “Non-uniformity correction of infrared images by midway equalization,” *Image Processing On Line*, vol. 2, pp. 134–146, 2012.
- [19] Y. Cao, M. Y. Yang, and C.-L. Tisse, “Effective strip noise removal for low-textured infrared images based on 1-d guided filtering,” *IEEE transactions on circuits and systems for video technology*, vol. 26, no. 12, pp. 2176–2188, 2015.
- [20] Y. Zhou, X. Li, X. Tang, J. Zhou, and L. Li, “A shutterless nonuniformity correction algorithm based on noise response model for tec-less uncooled infrared sensors,” *IEEE Sensors Journal*, 2023.
- [21] C. Zuo, Q. Chen, G. Gu, and W. Qian, “New temporal high-pass filter nonuniformity correction based on bilateral filter,” *Optical Review*, vol. 18, pp. 197–202, 2011.
- [22] Z. Li, T. Shen, and S. Lou, “Scene-based nonuniformity correction based on bilateral filter with reduced ghosting,” *Infrared Physics & Technology*, vol. 77, pp. 360–365, 2016.
- [23] Y. Chen, T.-Z. Huang, L.-J. Deng, X.-L. Zhao, and M. Wang, “Group sparsity based regularization model for remote sensing image stripe noise removal,” *Neurocomputing*, vol. 267, pp. 95–106, 2017.
- [24] Y. Chang, L. Yan, T. Wu, and S. Zhong, “Remote sensing image stripe noise removal: From image decomposition perspective,” *IEEE Transactions on Geoscience and Remote Sensing*, vol. 54, no. 12, pp. 7018–7031, 2016.
- [25] M. Bouali and S. Ladjal, “Toward optimal destriping of modis data using a unidirectional variational model,” *IEEE Transactions on geoscience and remote sensing*, vol. 49, no. 8, pp. 2924–2935, 2011.
- [26] Y. Chang, L. Yan, H. Fang, and C. Luo, “Anisotropic spectral-spatial total variation model for multispectral remote sensing image destriping,” *IEEE Transactions on Image Processing*, vol. 24, no. 6, pp. 1852–1866, 2015.
- [27] X. Kuang, X. Sui, Y. Liu, Q. Chen, and G. GU, “Single infrared image optical noise removal using a deep convolutional neural network,” *IEEE Photonics Journal*, vol. 10, no. 2, pp. 1–15, 2018.
- [28] P. Xiao, Y. Guo, and P. Zhuang, “Removing stripe noise from infrared cloud images via deep convolutional networks,” *IEEE Photonics Journal*, vol. 10, no. 4, pp. 1–14, 2018.
- [29] X. Kuang, X. Sui, Y. Liu, Q. Chen, and G. Guohua, “Single infrared image optical noise removal using a deep convolutional neural network,” *IEEE photonics Journal*, vol. 10, no. 2, pp. 1–15, 2017.
- [30] K. He, X. Zhang, S. Ren, and J. Sun, “Deep residual learning for image recognition,” in *Proceedings of the IEEE conference on computer vision and pattern recognition*, 2016, pp. 770–778.
- [31] Y. Chang, L. Yan, L. Liu, H. Fang, and S. Zhong, “Infrared aerothermal nonuniform correction via deep multiscale residual network,” *IEEE Geoscience and Remote Sensing Letters*, vol. 16, no. 7, pp. 1120–1124, 2019.
- [32] K. Xu, Y. Zhao, F. Li, and W. Xiang, “Single infrared image stripe removal via deep multi-scale dense connection convolutional neural network,” *Infrared Physics & Technology*, vol. 121, p. 104008, 2022.
- [33] S. Yuan, H. Qin, X. Yan *et al.*, “Arcnet: An asymmetric residual wavelet column correction network for infrared image destriping,” *arXiv preprint arXiv:2401.15578*, 2024. [Online]. Available: <https://arxiv.org/abs/2401.15578>
- [34] L. Chen, Y. Wang, and C. Zhang, “Spatial-spectral attention pyramid network for hyperspectral stripe restoration,” *IEEE Transactions on Geoscience and Remote Sensing*, vol. 62, pp. 1–17, 2024.
- [35] D. Ding, Y. Li, P. Zhao, K. Li, S. Jiang, and Y. Liu, “Single infrared image stripe removal via residual attention network,” *Sensors*, vol. 22, no. 22, p. 8734, 2022.
- [36] C. Wang, M. Xu, Y. Jiang, G. Zhang, H. Cui, L. Li, and D. Li, “Translation-snnet: A semisupervised hyperspectral image stripe noise removal based on transformer and cnn,” *IEEE Transactions on Geoscience and Remote Sensing*, vol. 60, pp. 1–14, 2022.
- [37] S. Yang, H. Qin, S. Yuan *et al.*, “Destripecyclegan: Stripe simulation cyclegan for unsupervised infrared image destriping,” *arXiv preprint arXiv:2402.09101*, 2024. [Online]. Available: <https://arxiv.org/abs/2402.09101>
- [38] R. Nishihara, L. Lessard, B. Recht, A. Packard, and M. Jordan, “A general analysis of the convergence of admm,” in *International conference on machine learning*. PMLR, 2015, pp. 343–352.
- [39] J. Chen, Y. Shao, H. Guo, W. Wang, and B. Zhu, “Destriping cmodis data by power filtering,” *IEEE Transactions on Geoscience and remote sensing*, vol. 41, no. 9, pp. 2119–2124, 2003.
- [40] J. G. Liu and G. L. K. Morgan, “Fft selective and adaptive filtering for removal of systematic noise in etm+ imageodesy images,” *IEEE Transactions on Geoscience and Remote Sensing*, vol. 44, no. 12, pp. 3716–3724, 2006.
- [41] J. Torres and S. O. Infante, “Wavelet analysis for the elimination of striping noise in satellite images,” *Optical Engineering*, vol. 40, no. 7, pp. 1309–1314, 2001.
- [42] J. Chen, H. Lin, Y. Shao, and L. Yang, “Oblique striping removal in remote sensing imagery based on wavelet transform,” *International Journal of Remote Sensing*, vol. 27, no. 8, pp. 1717–1723, 2006.
- [43] B. Münch, P. Trtik, F. Marone, and M. Stampanoni, “Stripe and ring artifact removal with combined wavelet—fourier filtering,” *Optics express*, vol. 17, no. 10, pp. 8567–8591, 2009.
- [44] H.-S. Jung, J.-S. Won, M.-H. Kang, and Y.-W. Lee, “Detection and restoration of defective lines in the spot 4 swir band,” *IEEE transactions on image processing*, vol. 19, no. 8, pp. 2143–2156, 2010.
- [45] L. Sun, R. Neville, K. Staenz, and H. P. White, “Automatic destriping of hyperion imagery based on spectral moment matching,” *Canadian Journal of Remote Sensing*, vol. 34, no. sup1, pp. S68–S81, 2008.
- [46] H. Zhang, W. Qian, Y. Xu, K. Zhang, X. Kong, and M. Wan, “Structural-information-awareness-based regularization model for infrared image stripe noise removal,” *Journal of the Optical Society of America A*, vol. 41, no. 9, pp. 1723–1737, 2024.
- [47] Z. He, Y. Cao, Y. Dong, J. Yang, Y. Cao, and C.-L. Tisse, “Single-image-based nonuniformity correction of uncooled long-wave infrared detectors: A deep-learning approach,” *Applied optics*, vol. 57, no. 18, pp. D155–D164, 2018.
- [48] S. Yuan, H. Qin, X. Yan, N. Akhtar, S. Yang, and S. Yang, “Irstdid-800: A benchmark analysis of infrared small target detection-oriented image destriping,” *IEEE Transactions on Geoscience and Remote Sensing*, 2024.
- [49] Y. Chang, L. Yan, H. Fang, S. Zhong, and W. L. HSI-DeNet, “Hyperspectral image restoration via convolutional neural network., 2018, 57,” DOI: <https://doi.org/10.1109/TGRS.2018.2867682>, 2018.
- [50] H. Shen and L. Zhang, “A map-based algorithm for destriping and inpainting of remotely sensed images,” *IEEE Transactions on Geoscience and Remote Sensing*, vol. 47, no. 5, pp. 1492–1502, 2008.
- [51] J.-L. Wang, T.-Z. Huang, T.-H. Ma, X.-L. Zhao, and Y. Chen, “A sheared low-rank model for oblique stripe removal,” *Applied mathematics and computation*, vol. 360, pp. 167–180, 2019.
- [52] X. Lu, Y. Wang, and Y. Yuan, “Graph-regularized low-rank representation for destriping of hyperspectral images,” *IEEE transactions on geoscience and remote sensing*, vol. 51, no. 7, pp. 4009–4018, 2013.

- [53] Y. Chang, L. Yan, and S. Zhong, "Transformed low-rank model for line pattern noise removal," in *Proceedings of the IEEE international conference on computer vision*, 2017, pp. 1726–1734.
- [54] G. H. Golub, A. Hoffman, and G. W. Stewart, "A generalization of the eckart-young-mirsky matrix approximation theorem," *Linear Algebra and its applications*, vol. 88, pp. 317–327, 1987.
- [55] G. W. Stewart, "On the early history of the singular value decomposition," *SIAM review*, vol. 35, no. 4, pp. 551–566, 1993.
- [56] Y. Tendero, S. Landeau, and J. Gilles, "Non-uniformity correction of infrared images by midway equalization," *Image Processing On Line*, vol. 2, pp. 134–146, 2012.
- [57] S.-i. Amari, "Backpropagation and stochastic gradient descent method," *Neurocomputing*, vol. 5, no. 4–5, pp. 185–196, 1993.
- [58] A. Beck and M. Teboulle, "A fast iterative shrinkage-thresholding algorithm for linear inverse problems," *SIAM journal on imaging sciences*, vol. 2, no. 1, pp. 183–202, 2009.
- [59] X. Jia, C. Zhu, M. Li, W. Tang, and W. Zhou, "Llvip: A visible-infrared paired dataset for low-light vision," in *Proceedings of the IEEE/CVF international conference on computer vision*, 2021, pp. 3496–3504.
- [60] A. Toet and M. A. Hogervorst, "Progress in color night vision," *Optical Engineering*, vol. 51, no. 1, pp. 010901–010901, 2012.
- [61] J. Korhonen and J. You, "Peak signal-to-noise ratio revisited: Is simple beautiful?" in *2012 Fourth international workshop on quality of multimedia experience*. IEEE, 2012, pp. 37–38.
- [62] Z. Wang, A. C. Bovik, H. R. Sheikh, and E. P. Simoncelli, "Image quality assessment: from error visibility to structural similarity," *IEEE transactions on image processing*, vol. 13, no. 4, pp. 600–612, 2004.
- [63] Q. Zeng, H. Qin, X. Yan, S. Yang, and T. Yang, "Single infrared image-based stripe nonuniformity correction via a two-stage filtering method," *Sensors*, vol. 18, no. 12, p. 4299, 2018.
- [64] ———, "Single infrared image-based stripe nonuniformity correction via a two-stage filtering method," *Sensors*, vol. 18, no. 12, p. 4299, 2018.
- [65] J. Zhu, X. Hu, L. Yang, H. Xu, N. Xu, and P. Zhang, "Study on the correction of sunlight pollution in mid-infrared image of fy-3c/virr," *Natl. Remote Sens. Bulletin*, vol. 25, pp. 803–815, 2021.
- [66] M. Hodosh, P. Young, and J. Hockenmaier, "Framing image description as a ranking task: Data, models and evaluation metrics," *Journal of Artificial Intelligence Research*, vol. 47, pp. 853–899, 2013.
- [67] L. Dong, J. Zhou, and Y. Y. Tang, "Effective and fast estimation for image sensor noise via constrained weighted least squares," *IEEE Transactions on Image Processing*, vol. 27, no. 6, pp. 2715–2730, 2018.
- [68] K. Dabov, A. Foi, V. Katkovnik, and K. Egiazarian, "Image denoising by sparse 3-d transform-domain collaborative filtering," *IEEE Transactions on image processing*, vol. 16, no. 8, pp. 2080–2095, 2007.
- [69] J. Guan, R. Lai, and A. Xiong, "Wavelet deep neural network for stripe noise removal," *IEEE Access*, vol. 7, pp. 44 544–44 554, 2019.
- [70] J. Liu, X. Fan, Z. Huang, G. Wu, R. Liu, W. Zhong, and Z. Luo, "Target-aware dual adversarial learning and a multi-scenario multi-modality benchmark to fuse infrared and visible for object detection," in *Proceedings of the IEEE/CVF Conference on Computer Vision and Pattern Recognition*, 2022, pp. 5802–5811.
- [71] L. Tang, J. Yuan, H. Zhang, X. Jiang, and J. Ma, "Piafusion: A progressive infrared and visible image fusion network based on illumination aware," *Information Fusion*, 2022.



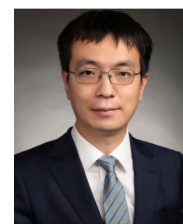
Chenhua Liu received his B.S. degree from Anhui University of Science and Technology. He is currently studying for a PhD at Beijing University of Information Science and Technology, Key Laboratory of Optoelectronic Testing Technology and Instrumentation of the Ministry of Education, and working as a staff member at Guangzhou Nansha Intelligent Photon Sensing Research Institute. His research interests include machine vision, ISP image processing, and RGB-D saliency detection.



Hao li received a bachelor's degree in computer science and technology from Beijing University of Information Science and Technology in 2023. Currently studying for a master's degree at Beijing University of Information Science and Technology. His research interests include infrared and visible image fusion and registration.



Maoyong Li received the B.S. degree from Yantai University, Yantai, China, in 2019. He is currently pursuing the Ph.D. degree with the school of Instrument Science and Optoelectronic Engineering, Beijing Information Science and Technology University, Beijing, China. His research interests include semantic segmentation and object detection.



Lei Deng received the B.S. degree from Beijing Institute of Technology University, Beijing, China, in 2009, and the Ph.D. degree from the Department of Automation, Tsinghua University, Beijing, in 2016. He was a Post-Doctoral Research Associate at Tsinghua University. He is currently a Lecturer at Beijing Information Science and Technology University, Beijing. His current research interests include image fusion, computer vision, and deep learning.



Mingli Dong received the M.Sc. degree from Hefei University of Technology, Hefei, China, in 1989, and the Ph.D. degree from Beijing Institute of Technology, Beijing, China, in 2009. Since 2008, she has been a Professor with Beijing Information Science and Technology University, Beijing, where she is the Dean of the School of Instrument Science and Opto-Electronics Engineering. Her research interests include sensing technology, photoelectric measurement technology, and precision measurement.



Lianqing Zhu received the M.S. degree from Hefei University of Technology, Hefei, China, in 1989, and the Ph.D. degree from Harbin Institute of Technology, Harbin, China, in 2013. Since 2004, he has been a Professor with Beijing Information Science and Technology University, Beijing, China. He is the Leader with the Yangtze River Scholars Innovation Team, National Key Talent, National Outstanding Mid-Aged Expert, and Science and Technology Beijing Leader Talent. His research interests include sensing technology, biomedical detection technology, and precision measurement.